

# Structural, magnetic and magneto optical properties of $\text{Fe}_3\text{O}_4/\text{NiO}$ bilayers on $\text{MgO}(001)$

Joachim Wollschläger<sup>a,b</sup>, Tobias Schemme<sup>a,b</sup>, Olga Kuschel<sup>a,b</sup>, Matthäus Witziok<sup>a,b</sup>, Timo Kuschel<sup>c</sup>, and Karsten Kuepper<sup>a,b</sup>

<sup>a</sup>Universität Osnabrück, Fachbereich Physik, Barbarastr. 7, Osnabrück, Germany

<sup>b</sup>Center of Physics and Chemistry of New Materials, Barbarastr. 7, Osnabrück, Germany

<sup>c</sup>Center of Spinelectronic Materials and Devices, Physics Department, Bielefeld University, Universitätstr. 25, Bielefeld, Germany

## ABSTRACT

Ultrathin magnetite ( $\text{Fe}_3\text{O}_4$ ) films are attractive for applications in the field of spintronics due to their ferrimagnetic behavior with assumed high degree of spin polarized electrons at the Fermi energy. For these applications, it is necessary to form epitaxial bilayer structure combining ferrimagnetic magnetite with an antiferromagnetic layer. Therefore, here we study  $\text{Fe}_3\text{O}_4/\text{NiO}$  bilayers on  $\text{MgO}(001)$  substrates. Bilayers grown by reactive molecular beam epitaxy are stoichiometric and have well-developed surface and interface structures. The  $\text{NiO}$  layers are laterally pinned to the structure of the  $\text{MgO}(001)$  substrate while the magnetite films gradually relax. The interfaces show smooth morphologies and the films have very homogeneous film thickness necessary for spintronic applications. The magnetic and magneto optical properties of the  $\text{Fe}_3\text{O}_4/\text{NiO}$  bilayers were probed by the magneto optical Kerr effect. Compared to single  $\text{Fe}_3\text{O}_4$  layers on  $\text{MgO}(001)$ , the bilayers show complicated ferrimagnetic behavior depending on the azimuthal direction of the external applied field. The coercive field of the bilayers, however, is increased with the coercive field of single layer  $\text{Fe}_3\text{O}_4/\text{MgO}(001)$  structures making the  $\text{Fe}_3\text{O}_4/\text{NiO}$  bilayers attractive for spintronic applications.

**Keywords:** magnetite,  $\text{Fe}_3\text{O}_4$ ,  $\text{NiO}$ ,  $\text{MgO}$ , exchange bias, synchrotron radiation, x-ray diffraction, x-ray reflectometrie, magneto optic Kerr effect, low-energy electron diffraction, x-ray photoelectron spectroscopy, XRD, XRR, MOKE, LEED, XPS

## 1. INTRODUCTION

The investigation of physical properties of spin polarized materials is of extreme relevance in the field of spintronics spin, e.g., to develop spin filters. Here, the halfmetallic iron oxide magnetite ( $\text{Fe}_3\text{O}_4$ ) gained reasonable attraction since 100% spin polarization at the Fermi level has been predicted.<sup>1</sup>

$\text{Fe}_3\text{O}_4$  has inverse spinel structure for the bulk where the different Fe cations  $\text{Fe}^{2+}$  and  $\text{Fe}^{3+}$ , which are ingredients in magnetite with the stoichiometry  $\text{Fe}^{2+}:\text{Fe}^{3+} = 1:2$ , are distributed on different sublattices with differently coordinated lattice sites. Tetrahedral lattice sites are occupied by  $\text{Fe}^{3+}$  cations while octahedral lattice sites are occupied by both  $\text{Fe}^{2+}$  and  $\text{Fe}^{3+}$  cations with equal parts. This distribution of cations results to antiferromagnetic coupling between the  $\text{Fe}^{3+}$  cations on the octahedral and the  $\text{Fe}^{3+}$  cations on tetrahedral sublattices so that the remaining magnetic momentum of magnetite is created by  $\text{Fe}^{2+}$  cations on octahedral lattice sites. Therefore,  $\text{Fe}_3\text{O}_4$  is a ferrimagnet with  $4.07 \mu_B$  magnetic momentum per formula unit and a Curie temperature of 860 K.

Furthermore, these ferrimagnetic properties makes magnetite very attractive as material for spintronic all-oxide devices.<sup>2</sup> For instance,  $\text{Fe}_3\text{O}_4$  may be used as ferrimagnetic material for electrodes in Magnetic Tunnel Junctions (MTJ) with applications as Tunnel Magneto Resistor (TMR) for data storage devices. Here, the key feature is the spin dependent tunnel transport between the ferrimagnetic electrodes. Electrons can tunnel if the magnetic momenta of the electrodes are parallel while this is not possible for anti-parallel arrangement of the

---

Further author information: (Send correspondence to J.W.)

J.W.: E-mail: jwollsch@uos.de, Telephone: +49 541 969 2651

magnetic momenta.<sup>3-6</sup> Therefore, in principle, it is possible to build logic devices with Fe<sub>3</sub>O<sub>4</sub> electrodes which are separated by ultrathin tunneling barriers, e.g., MgO as demonstrated previously.<sup>7</sup>

Using identical materials for both electrodes, however, one has to "harden" one of the electrodes so that both electrodes do not have the same switching fields. One possibility to increase the strength of switching fields is to combine the ferrimagnetic material with an anti-ferromagnetic material since the ferrimagnetic properties are modified due to ex-change bias field at the ferrimagnetic/anti-ferromagnetic (F/AF) interfaces.<sup>8</sup> Here, NiO is a well-suited candidate since its Neel temperature of 523 K is higher than room temperature.

It is attractive to combine Fe<sub>3</sub>O<sub>4</sub> and NiO since both materials are lattice matched. Taking bulk values, the lattice mismatch of Fe<sub>3</sub>O<sub>4</sub> (cubic lattice constant of 839.6 pm) is only 0.5% compared to NiO if one doubles the cubic lattice constant of 417.7 pm. Furthermore, the high quality matching of both materials is certified since both bulk materials have cubic symmetry (inverse spinel for Fe<sub>3</sub>O<sub>4</sub> and rocksalt structure for NiO) and the oxygen sublattice in both materials has fcc structure. Therefore, a common oxygen sublattice can be continued crossing the Fe<sub>3</sub>O<sub>4</sub>/NiO interface and the bilayers have excellent structural properties.<sup>9</sup>

In addition, it is advantageous to grow Fe<sub>3</sub>O<sub>4</sub>/NiO bilayers on MgO(001) which also has rocksalt structure and is an insulator with 8 eV bandgap. The lattice matching of MgO (cubic lattice constant of 421.2 pm) is 0.3% and 0.8% with respect to Fe<sub>3</sub>O<sub>4</sub> and NiO, respectively. Previously, it has been demonstrated that high quality Fe<sub>3</sub>O<sub>4</sub> films can be grown on MgO(001) substrates.<sup>10</sup> These films show excellent ferrimagnetic properties if appropriate growth conditions are used to build well-ordered magnetite films.<sup>11</sup>

Therefore, we present here our studies on Fe<sub>3</sub>O<sub>4</sub>/NiO bilayers on MgO(001) substrates. We characterized *in-situ* interfacial and surface properties of the individual oxide films directly after deposition of the film. Further *ex-situ* studies have been performed to characterize the structural and magnetic as well as magneto-optical properties of the bilayer structures.

## 2. EXPERIMENTAL

The sample preparation was carried out in an ultra high vacuum chamber system consisting of a preparation chamber (base pressure of 10<sup>-8</sup> mbar) and an analysis chamber (base pressure of 10<sup>-10</sup> mbar).

Before film deposition the MgO(001) substrates (CrysTec) were cleaned by annealing them at 400 °C in 10<sup>-4</sup> mbar O<sub>2</sub> for 60 min. After sample transfer to the analysis chamber, the cleanness of the surface (especially removing of carbon contaminants) was proved by X-ray Photoelectron Spectroscopy (XPS). The XPS system operates with an hemispherical analyzer and an Al K<sub>α</sub> x-ray anode (1486.6 eV). Furthermore, the surface quality was characterized by Low Energy Electron Diffraction (LEED).

Oxide films were deposited by means of Reactive Molecular Beam Epitaxy (RMBE) evaporating metals from a rod by electron bombardment in oxygen atmosphere. The O<sub>2</sub> pressure, however, was adjusted to obtain the intended oxide stoichiometry. The deposition rate was controlled with a quartz microbalance mounted close to the evaporator. The quartz microbalance was calibrated with test structures determining their film thickness by means of X-Ray Reflectometry (XRR).

NiO films were deposited at 250 °C in 10<sup>-5</sup> mbar O<sub>2</sub>. Here, we used a growth rate of 0.7(±0.1) nm/min. For the deposition of the Fe<sub>3</sub>O<sub>4</sub> films, 250 °C deposition temperature was used, too, while the O<sub>2</sub> pressure was reduced to 5×10<sup>-6</sup> mbar and the growth rate increased to 7(±1) nm/min to obtain the intended Fe<sub>3</sub>O<sub>4</sub> stoichiometry and high film quality.<sup>11</sup> After each deposition step, the surface structure and the stoichiometry of the surface near region was determined by means of LEED and XPS, respectively. We have to emphasize that the information depth of the Al K<sub>α</sub> radiation is approximately 5 nm due to the limited escape depth of photoelectrons and, therefore, we could only detect the surface near stoichiometry of the intermediate uncovered NiO film or the top Fe<sub>3</sub>O<sub>4</sub> film deposited on the NiO film. In principle, it is not possible to determine the stoichiometry of the entire bilayer structure using soft x-ray photoelectron spectroscopy.

After sample preparation the samples were exposed to ambient conditions for different *ex situ* experiments. The film thickness and structure of the films was analyzed by means of synchrotron radiation using both Synchrotron Radiation X-Ray Reflectometry (SR-XRR) and Synchrotron Radiation X-Ray Diffraction (SR-XRD), respectively. Both SR-XRR and SR-XRD experiments were carried out at Deutsches Elektronen-Synchrotron

(DESY), Hamburg at PETRA III beamline P08. This is an undulator beamline with a high heat-load double-crystal monochromator and large-offset monochromator to separate the beamline from the adjacent beamline. At the endstation a Kohzu 4S+2D type diffractometer is installed.<sup>12</sup> A Mythen array detector<sup>13</sup> was used due to its higher dynamic range and the capability of creating reciprocal space maps (RSM) within a shorter period of time compared to a point detector.

The magneto optical properties of the films were analyzed by means of the Magneto Optical Kerr Effect (MOKE) using a setup reported earlier.<sup>14</sup> The MOKE measurements were performed in the longitudinal setup geometry using a HeNe laser ( $\lambda = 632.8 \text{ nm}$ ) at an incidence angle of  $45^\circ$ . A photoelastic modulator with a modulation frequency of  $f = 42 \text{ kHz}$  is used to modulate the polarization of the reflected beam. The intensity of the reflected laser beam is detected by a photo diode after its modulated polarization signal has been converted into an intensity signal by an analyzer (polarizer at  $45^\circ$ ). We used the intensity of the  $2f$ -signal (using the lock-in technique), which is proportional to the Kerr rotation angle within the small angle approximation, to characterize the magnetization of the samples.

### 3. RESULTS AND DISCUSSION

#### 3.1 In-situ Characterization: XPS and LEED

Having prepared the MgO(001) substrate, NiO films have been deposited in a first step followed by preparation of  $\text{Fe}_3\text{O}_4$  films in a second step. After each step the sample has been transferred to the analysis chamber. Here, the samples were studied by both XPS and LEED.

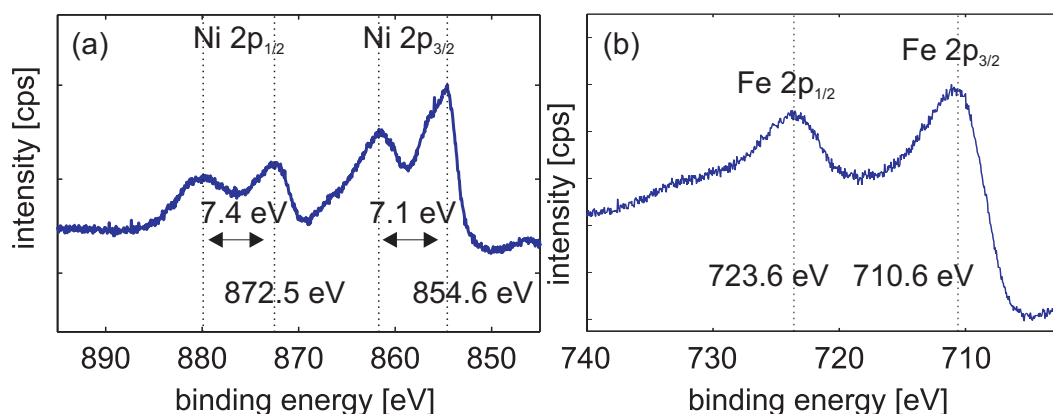


Figure 1. 2p photoelectron spectra of (a) NiO and (b)  $\text{Fe}_3\text{O}_4$ . Both spectra show the splitting in  $2p_{3/2}$  photoelectron peaks (high binding energy) and  $2p_{1/2}$  photoelectron peaks (low binding energy). Additional charge transfer peaks can be observed for Ni 2p due to its mono 2+ valency while no apparent charge transfer peaks can be seen for  $\text{Fe}_3\text{O}_4$  due to its mixed valency.

Fig.1 shows typical Ni 2p and Fe 2p spectra recorded after deposition of (a) a NiO film on MgO(001) and (b) a  $\text{Fe}_3\text{O}_4$  film on NiO/MgO(001). The spectra had to be calibrated due to charging of the samples. For this purpose, we used the O 1s photoelectron peak assuming that the O 1s electrons have 530 eV binding energy.<sup>15</sup> No thickness dependent charging effects could be observed.

The Ni 2p spectra presented in Fig.1(a) consist of the Ni  $2p_{3/2}$  peak at 854.6 eV and the Ni  $2p_{1/2}$  peak at 872.5 eV with their corresponding satellites at about 7 eV higher binding energies. The measured Ni 2p spectra agree excellently with Ni 2p spectra for NiO reported in literature<sup>16–18</sup> demonstrating that the NiO films have the aimed stoichiometry.

The XP spectra of the Fe 2p region of all samples exhibit the same shape. The Fe  $2p_{3/2}$  and the Fe  $2p_{1/2}$  photoelectron peaks are located at binding energies of 710.6 eV and 723.6 eV, respectively. In principle, additional charge transfer satellites are observed for iron oxides either exclusively with  $\text{Fe}^{2+}$  ingredients (FeO) or exclusively with  $\text{Fe}^{3+}$  constituents ( $\text{Fe}_2\text{O}_3$ ).<sup>15,19</sup> These charge transfer satellites, however, overlap for  $\text{Fe}_3\text{O}_4$  having mixed

constituents. Thus, for stoichiometric  $\text{Fe}_3\text{O}_4$ , no apparent satellite can be observed in the Fe 2p spectrum.<sup>15,19</sup> Therefore, the Fe 2p spectrum presented in Fig.1(b) verifies the  $\text{Fe}_3\text{O}_4$  stoichiometry of the deposited iron oxide films.

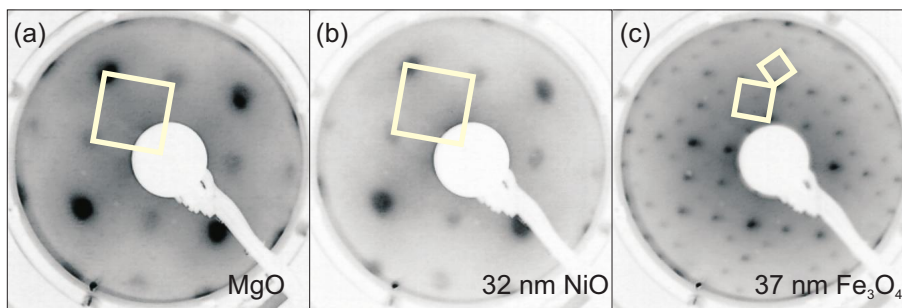


Figure 2. LEED pattern recorded at 135 eV for (a) MgO(001) substrate, (b) NiO film on MgO(001) and (c)  $\text{Fe}_3\text{O}_4$  film on NiO/MgO(001). The squares denote the reciprocal unit cell. While the one-to-one lattice matched NiO/MgO(001) can be seen comparing (a) and (b) the magnetite show a half-sized reciprocal unit cell due to its (almost) doubled cubic bulk unit cell. The additional  $(\sqrt{2} \times \sqrt{2})\text{R}45^\circ$  superstructure confirms the formation of  $\text{Fe}_3\text{O}_4$ .

In addition, LEED experiments were performed on the surfaces of the MgO(001) substrate and the deposited oxide films for electron energies varying from 80 eV to 200 eV. For 135 eV electrons, LEED pattern for the MgO(001) substrate, the NiO film and the  $\text{Fe}_3\text{O}_4$  film are presented in Fig.2.

Fig.2(a) shows the diffraction pattern of the MgO(001) surface. In addition, the reciprocal surface unit cell of the MgO(001) surface with square symmetry is presented (cf. square = reciprocal surface unit cell). This diffraction pattern as well as the bright diffraction spots confirm the high quality of the MgO(001) surface.

After deposition of the NiO film, the LEED pattern of Fig.2(b) is obtained. The symmetry of the diffraction pattern shows that a NiO(001) surface with square symmetry is formed (cf. square). Compared to the MgO(001) pattern the diffraction spots are located at almost identical positions while the intensities of the diffraction peaks are usually different compared to the LEED result from the MgO(001) substrate. This effect can be explained by the very similar lattice constant of NiO which is lattice matched to the MgO(001) substrate. Therefore, the comparison of the LEED patterns of the MgO(001) substrate and the NiO(001) film confirms cube-on-cube epitaxial growth of the NiO film. The intensity variations, however, are due to dynamical processes for electron diffraction. Furthermore, the bright diffraction spots verify that the NiO(001) films are of high quality.

Fig.2(c) presents a LEED pattern obtained after deposition of an iron oxide film on NiO(001)/MgO(001). The pattern shows again the square symmetry of a cubic crystalline structure. Compared to the LEED pattern obtained from both the MgO(001) substrate or from the NiO(001) film, however, additional diffraction spots are observed. On one hand, these additional diffraction peaks are caused by the larger bulk unit cell of the the iron oxide film pointing to the formation of an  $\text{Fe}_3\text{O}_4(001)$  film or an  $\text{Fe}_2\text{O}_3(001)$  film with almost doubled cubic bulk lattice constants compared to NiO and MgO. Diffraction peaks due to the larger lattice constant are demonstrated by the larger of the two squares (showing the  $(1 \times 1)$  reciprocal surface unit cell) in Fig.2(c). This has (almost) half side length compared to the reciprocal unit cells (squares) marked in Fig.2(a) and (b). Therefore, the formation of FeO can be excluded since, like MgO and NiO, FeO has rocksalt structure and also has a (bulk) lattice constant very similar to NiO and MgO. On the other hand, the LEED pattern also shows an additional  $(\sqrt{2} \times \sqrt{2})\text{R}45^\circ$  superstructure which is reported for  $\text{Fe}_3\text{O}_4$  but excluded for  $\text{Fe}_2\text{O}_3$ .<sup>20</sup> Therefore, the LEED pattern obtained from the iron oxide film point to the formation of  $\text{Fe}_3\text{O}_4$  film, too.

In summary, combining XPS and LEED experiments it is confirmed that a crystalline and stoichiometric  $\text{Fe}_3\text{O}_4(001)$  film has been deposited on a crystalline and stoichiometric NiO(001) film.

### 3.2 Bulk Structure: SR-XRR and SR-XRD

SR-XRR studies have been performed with synchrotron radiation using 10.5 keV x-ray photons (corresponding wavelength  $\lambda = 118$  pm) and the received data are presented in Fig.3. All curves show clear intensity oscillations

which are related to interference effects between partial waves reflected at the different interfaces of the bilayer structure. Some of the curves show "beating" effects with superposition of a long and a short period. This effect points to different film thicknesses of the  $\text{Fe}_3\text{O}_4$  film and the NiO film. Since we aimed here for a constant NiO film thickness while the  $\text{Fe}_3\text{O}_4$  film thickness was varied, on first sight, the constant periodicity observed in all curves can be attributed to the (almost) constant NiO film thickness while the second decreasing periodicity from the top curve to the bottom curve can be attributed to the increasing  $\text{Fe}_3\text{O}_4$  film thickness.

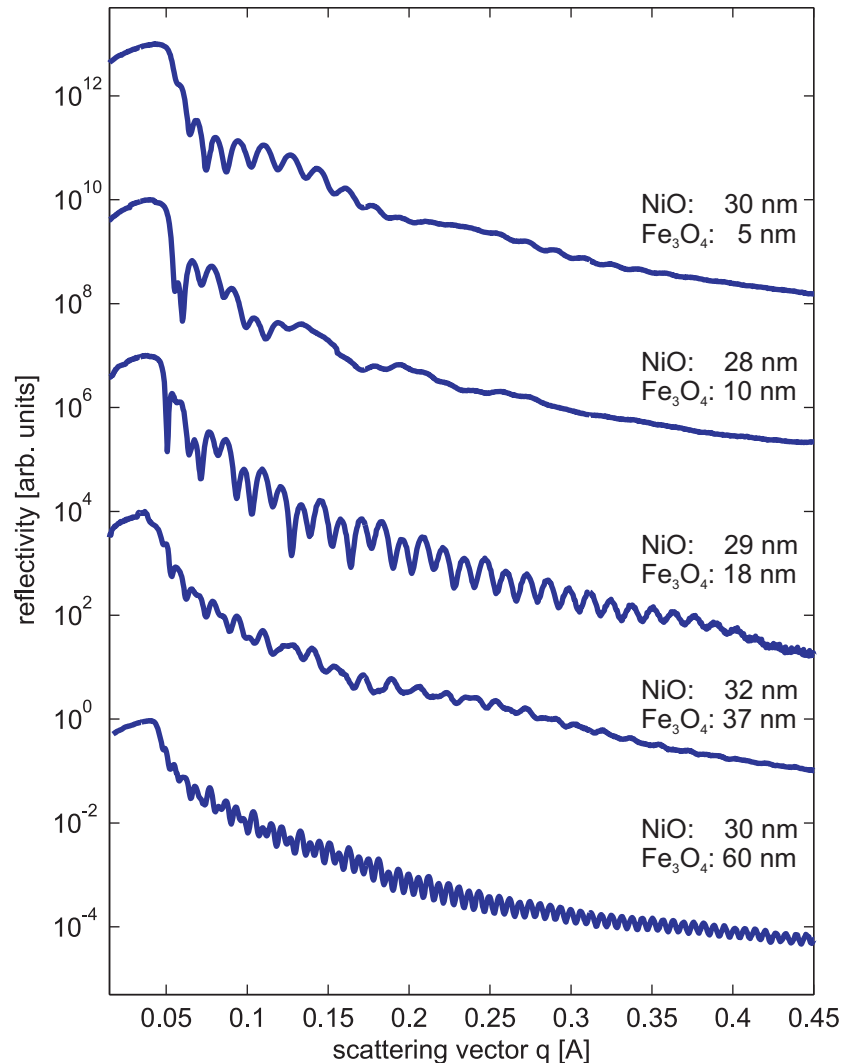


Figure 3. SR-XRR data for  $\text{Fe}_3\text{O}_4/\text{NiO}$  bilayers with (almost) constant NiO film thickness and increasing  $\text{Fe}_3\text{O}_4$  film thickness (from top to bottom). Intensity oscillations (Kiessig fringes) are caused by interference of the partial waves reflected at the different interfaces. While a clear "beating" effect can be observed for the thinnest  $\text{Fe}_3\text{O}_4$  films, the decreased periodicity of the intensity oscillations is caused by the increased  $\text{Fe}_3\text{O}_4$  film thickness.

However, one has to model the data to obtain better insight in the bilayer structure. Therefore, calculations have been performed based on the multilayer model proposed by Parratt<sup>21</sup> to fit the experimental data. Here, we assume the stacking of  $\text{Fe}_3\text{O}_4/\text{NiO}/\text{MgO}(001)$  and we vary the film thicknesses and the optical constants  $n$  of the individual layers. In addition, effects due to interface roughness have been included following the model of Croce and Nevot.<sup>22</sup> We obtain that the thickness of the samples discussed here is  $30(\pm 2)$  nm while the  $\text{Fe}_3\text{O}_4$  thickness increases from 5 nm to 60 nm as noted in Fig.3.

The well developed intensity oscillations demonstrate that the interfaces are very smooth with very small



roughness. Closer inspection of the data (see above) reveal the rms roughness  $\sigma_{\text{NiO-Fe}_3\text{O}_4} = 0.6(\pm 0.1)$  nm of the NiO-Fe<sub>3</sub>O<sub>4</sub> interface and the rms roughness  $\sigma_{\text{Fe}_3\text{O}_4} < 0.2$  nm of the surface of the Fe<sub>3</sub>O<sub>4</sub> film.

Further information from the reflectivity analysis can be obtained for the optical constants  $n$  of the materials used in the bilayer stacks. For x-rays, the optical constant  $n = 1 - \delta$  depends on the electron density  $n_e$  via

$$\delta = \frac{r_e n_e \lambda^2}{2\pi}. \quad (1)$$

Here,  $r_e$  denotes the classical electron radius  $r_e = 282$  fm. Consequently, x-rays are totally reflected for glancing angles  $\theta$  smaller than the critical angle  $\theta_c = \sqrt{2\delta}$  (equivalent to the critical scattering vector  $q_c = 4\pi \sin \theta_c / \lambda$  perpendicular to the interface).<sup>23</sup> The critical angles for the studied samples can nicely be seen in Fig.3 with drastically decreasing intensity if the scattering vector is beyond the critical scattering vector.

As stated above, one has to fit the entire reflectivity curve to obtain reliable data of the optical constants of both constituents of the Fe<sub>3</sub>O<sub>4</sub>/NiO bilayers. The detailed XRR analysis of our data revealed  $\delta_{\text{Fe}_3\text{O}_4}^{\text{film}} = 9.36(\pm 0.04) \times 10^{-6}$  and  $\delta_{\text{NiO}}^{\text{film}} = 1.20(\pm 0.02) \times 10^{-5}$  for the Fe<sub>3</sub>O<sub>4</sub> and NiO films, respectively. Comparing these values with bulk values of  $\delta_{\text{Fe}_3\text{O}_4}^{\text{bulk}} = 9.25 \times 10^{-6}$  and  $\delta_{\text{NiO}}^{\text{bulk}} = 1.20 \times 10^{-5}$  for the Fe<sub>3</sub>O<sub>4</sub> and NiO films, respectively, we obtain excellent agreement for NiO film but a slightly increased value for the Fe<sub>3</sub>O<sub>4</sub> films. Following eq.(1), the increased value of the iron oxide layer points to an increased electron density. Comparing the  $\delta$  values obtained here with values of iron oxide with other stoichiometries ( $\delta_{\text{FeO}}^{\text{bulk}} = 1.05 \times 10^{-5}$ ,  $\delta_{\text{Fe}_2\text{O}_3}^{\text{bulk}} = 8.74 \times 10^{-6}$ ), the increased value of  $\delta$  value points to a slightly increased Fe content or to an equivalent small deficiency of lattice oxygen.

XRD studies are well-suited to gain insight in the structure of the bilayers and, therefore, to investigate relaxation processes. For the bilayer system Fe<sub>3</sub>O<sub>4</sub>/NiO/MgO(001) studied here, however, the resolution of lab based XRD experiments is too low since the (bulk) lattice constants of the contributing materials are too similar so that Bragg peaks overlap significantly. This effect is enhanced compared to diffraction at bulk since diffraction peaks from ultrathin films are broadened due to finite size effects. Therefore, the signal obtained from films is usually strongly overlapped by the substrate signal and hidden in the wings of the substrate Bragg peaks. Thus, one has to perform high resolution XRD experiments with synchrotron radiation and, for this purpose, we used the high resolution beamline P08 of PETRA III at DESY (Deutsches Elektronensynchrotron).

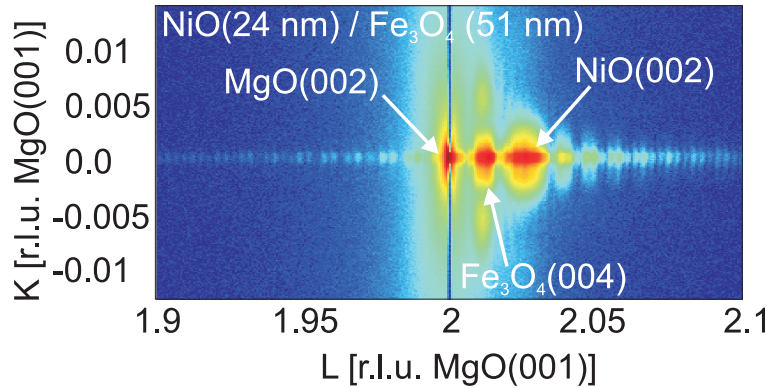


Figure 4. Reciprocal space ( $HL$ ) map close to the  $(002)_S$  Bragg peaks of the MgO(001) substrate and the NiO(001) film. Between these Bragg peak on finds the Fe<sub>3</sub>O<sub>4</sub>(004)<sub>S</sub> Bragg peak. In addition, Laue fringes are clearly seen along the  $(00L)$  CTR due to the homogeneous film thickness.

Fig.4 shows a Reciprocal Space Map (RSM) recorded from a bilayer sample with a 51 nm Fe<sub>3</sub>O<sub>4</sub> film deposited on a 24 nm NiO film. The RSM is recorded in the ( $KL$ ) plane and the 3D Bragg conditions due to diffraction at the 3D crystal structure are marked. One can clearly see that the Bragg peaks of the MgO substrate as well as of both oxide films can be distinguished well. In addition, one can see a series of intensity maxima with smaller intensities (Laue fringes) due to the formation of very homogeneous epitactical films.

Different to bulk diffraction where 3D Bragg conditions have to be obeyed to have constructive interference, it is important for surfaces and films that the diffraction signal is continuously distributed vertical to surfaces and interfaces. Thus, one has only two strict in-plane Laue conditions while the vertical component is less strict and one obtains 2D Bragg rods or Crystal Truncation Rods (CTRs) instead of 3D Bragg points.

Therefore, we measured these CTRs denoted by  $(HKL)$  with integer values of  $H$  and  $K$  but continues values of  $L$  which denotes the vertical scattering vector  $q_{\perp}$  scaled with layer distance  $c_{\text{MgO}}$  of the MgO substrate via  $L = c_{\text{MgO}} q_{\perp} / 2\pi$ . For the surface diffraction notation used here, the substrate Bragg peak  $\text{MgO}(002)_S$  (cf. Fig.4) is equivalent to the  $\text{MgO}(004)_B$  Bragg peak in bulk notation (scaled to the size of the cubic bulk unit cell). Equivalently, the  $\text{NiO}(002)_S$  and  $\text{Fe}_3\text{O}_4(004)_S$  (cf. Fig.4) are  $\text{NiO}(004)_B$  and  $\text{Fe}_3\text{O}_4(008)_B$  Bragg peaks, respectively, in bulk notation.

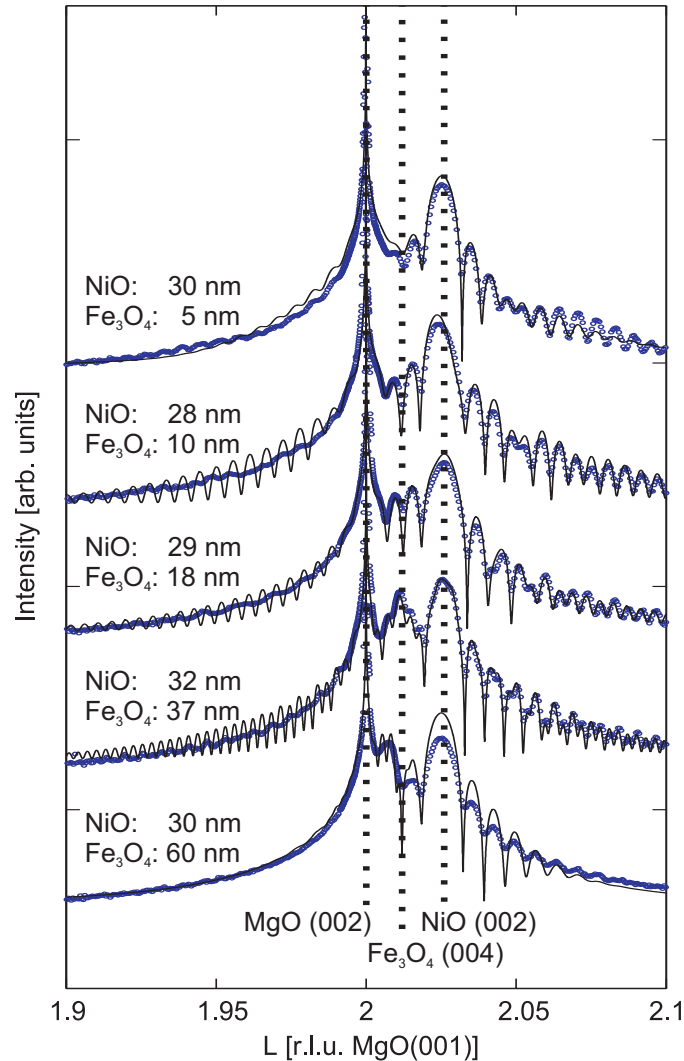


Figure 5.  $(00L)$  CTRs for  $\text{Fe}_3\text{O}_4/\text{NiO}$  bilayers with constant NiO film thickness and increasing  $\text{Fe}_3\text{O}_4$  film thickness (from top to bottom). Experimental data are shown in blue, calculated curves (using the kinematic approximation) are shown in black. While the Bragg peaks due to the MgO substrate and the NiO film are always clearly seen the  $\text{Fe}_3\text{O}_4$  Bragg peak is often modified due to strong interference effects.

For specular diffraction (scattering vector perpendicular to the surface, no component of the scattering vector parallel to the surfaces and interfaces), Fig.5 shows the diffractograms of the  $(00L)$  CTR for the samples studied

before by XRR (s. above). We used the diffraction signal close to the  $\text{MgO}(002)_\text{S}$  Bragg peak to separate better the Bragg peaks of the different layers from the substrate signal. The dashed lines in Fig.5 show the position of the NiO Bragg peaks and demonstrate that the NiO films completely adopt the lateral structure of the MgO substrate (laterally expanded NiO film due to pseudomorphic film growth, cf. also Fig.6).

Therefore, the film structure has to be compressed in vertical direction. Following continuum elasticity theory, the relative compression is given by

$$\frac{\Delta c_{\text{NiO}}}{c_{\text{NiO}}^{\text{bulk}}} = \frac{2\nu}{\nu - 1} \frac{\Delta a_{\text{NiO}}}{a_{\text{NiO}}^{\text{bulk}}} \quad (2)$$

as developed for tetragonally distorted films.<sup>24</sup> Here,  $\nu$  denotes the Poisson ratio. Furthermore,  $\Delta c_{\text{NiO}} = c_{\text{NiO}}^{\text{film}} - c_{\text{NiO}}^{\text{bulk}}$  and  $\Delta a_{\text{NiO}} = a_{\text{NiO}}^{\text{film}} - a_{\text{NiO}}^{\text{bulk}}$  denote the vertical and lateral film strain, respectively, while  $a_{\text{NiO}}^{\text{film}}$  and  $a_{\text{NiO}}^{\text{bulk}}$  are the lateral lattice constants of the strained NiO film and of the (unstrained) NiO bulk, respectively. Assuming that the Poisson ratio is  $\nu = 0.21$  (bulk value),<sup>25</sup> the XRD data show that the NiO film is completely strained (cf. Fig.6).

Different from the NiO diffraction signal, on first sight, no clear  $\text{Fe}_3\text{O}_4$  Bragg peaks can be seen in Fig.5 although its thickness is larger than the NiO film thickness in some cases. This effect is caused by strong interference effects and enhanced due to the fact that the  $\text{Fe}_3\text{O}_4$  Bragg peak has a middle position between the MgO and NiO Bragg peaks. Therefore, we had to perform a complete diffraction analysis based on the kinematic approximation. The result of the adjusted fit curves are presented as black curves in Fig.5. The calculated curves excellently reproduce the experimental data including the intensity oscillations (Laue fringes) due to the finite thickness of the both oxide films. It has to be emphasized that the Laue fringes indicate that the interfaces of the bilayer systems are very smooth.

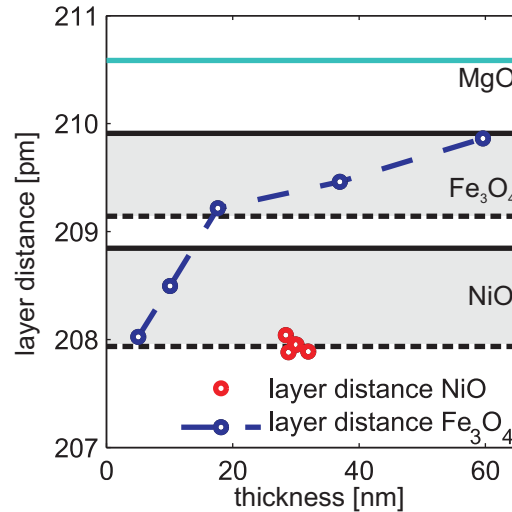


Figure 6. Dependence of the  $\text{Fe}_3\text{O}_4(001)$  layer distance on the film thickness. Initially the  $\text{Fe}_3\text{O}_4$  film suffers strong tensile strain and the vertical layer distance is stronger reduced than expected (dashed line at the bottom of the grey field for  $\text{Fe}_3\text{O}_4$ ). The  $\text{Fe}_3\text{O}_4$  film relaxes gradually with increasing film thickness. The NiO film, however, is completely strained.

The vertical layer distances  $c_{\text{Fe}_3\text{O}_4}^{\text{film}}$  determined from the complete XRD analysis for the different  $\text{Fe}_3\text{O}_4$  films are presented in Fig.6. Obviously, the vertical layer distance increases with increasing film thickness. For the thinnest  $\text{Fe}_3\text{O}_4$  film we obtain the vertical layer distance of 208 pm. This value is smaller than the value expected for a pseudomorphic film following eq.(2) and assuming the bulk value  $\nu = 0.356$  for the Poisson ratio<sup>26</sup> (cf. grey shaded region in Fig.6). For the 60 nm  $\text{Fe}_3\text{O}_4$  film, however, the vertical lattice constant of the  $\text{Fe}_3\text{O}_4$  film agrees well with the bulk value. Therefore, different to the completely strained NiO film, the  $\text{Fe}_3\text{O}_4$  film seems to relax continuously until it is completely relaxed for 60 nm film thickness.



### 3.3 Magneto optical properties: MOKE

Having clarified structural properties of  $\text{Fe}_3\text{O}_4/\text{NiO}$  bilayers on  $\text{MgO}(001)$ , we studied also the magnetic and magneto optical of *selected*  $\text{Fe}_3\text{O}_4/\text{NiO}$  bilayers (cf. Tab.1) by MOKE which is sensitive to the magnetization of the magnetite film. Here, we applied the external magnetic field in-plane to the film and also in the plane of reflection of the laser beam (Longitudinal Magneto Optical Kerr Effekt, LMOKE). Furthermore, the azimuthal angle of the  $\text{Fe}_3\text{O}_4/\text{NiO}/\text{MgO}(001)$  structures was varied to obtain deeper insight in the anisotropic behavior of the magnetization eventually induced by the crystalline structure.

Table 1. Samples used for MOKE experiments

sample	$\text{Fe}_3\text{O}_4$ thickness	NiO thickness
A	36nm	-
B	117nm	-
C	26nm	45nm
D	37nm	14nm
E	37nm	32nm
F	60nm	30nm

Applying the external field in  $[100]$  direction, Fig.7 shows the Kerr angle depending on the external field for three different samples:  $\text{Fe}/\text{MgO}(001)$ ,  $\text{Fe}_3\text{O}_4/\text{MgO}(001)$  and  $\text{Fe}_3\text{O}_4/\text{NiO}/\text{MgO}(001)$ . Clearly, the highest Kerr angle can be observed for large external magnetic fields  $\mu_0 H$  for the Fe film. Compared to this the  $\text{Fe}_3\text{O}_4/\text{MgO}(001)$  structure shows the smallest Kerr angle while the Kerr angle lies in between for the  $\text{Fe}_3\text{O}_4/\text{NiO}$  bilayer on  $\text{MgO}(001)$ .

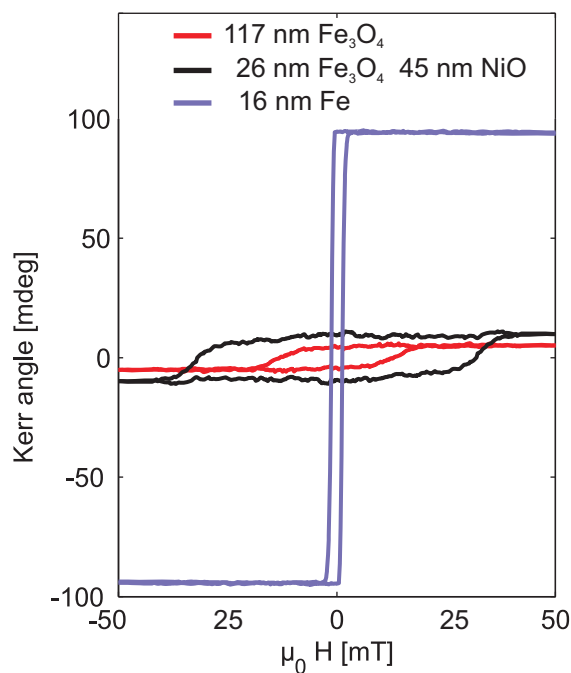


Figure 7. Hysteresis for ultrathin films of (a) 16 nm Fe, (b) 26 nm  $\text{Fe}_3\text{O}_4$  on 45 nm NiO and (c) 117 nm  $\text{Fe}_3\text{O}_4$ . The Fe film shows large saturation Kerr angles but small coercive fields. The angles are drastically reduced for the  $\text{Fe}_3\text{O}_4$  films while the coercive fields are increased with the largest coercive field for the  $\text{Fe}_3\text{O}_4/\text{NiO}$  bilayer.

Obviously, the dependence of the magnetization  $M$  (proportional to the Kerr angle) on the external field shows hysteresis behaviour. This can be characterized by the squareness  $M_r/M_s$  where  $M_r$  and  $M_s$  denote the remanent magnetization and the saturation magnetization, respectively. Qualitatively, all samples have a large remanence and show well developed squarenesses.

Regarding the coercive field  $H_c$ , however, the results are different. Here, the Fe film shows the smallest coercive field of  $\mu_0 H_c^{\text{Fe}} = 1.2 \text{ mT}$ . The coercive field increases drastically for the single  $\text{Fe}_3\text{O}_4$  film ( $\mu_0 H_c^{\text{Fe}_3\text{O}_4} = 13 \text{ mT}$ ) and assumes the largest value of  $\mu_0 H_c^{\text{Fe}_3\text{O}_4/\text{NiO}} = 32 \text{ mT}$  for the  $\text{Fe}_3\text{O}_4/\text{NiO}$  bilayer.

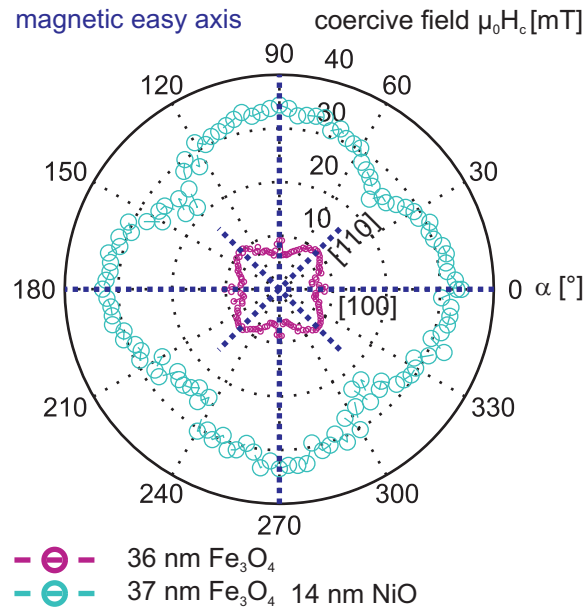


Figure 8. Comparison of the azimuthal dependence of the coercive field of a single  $\text{Fe}_3\text{O}_4$  layer and a  $\text{Fe}_3\text{O}_4/\text{NiO}$  bilayer. The coercive field of the  $\text{Fe}_3\text{O}_4/\text{NiO}$  bilayer is generally larger than the coercive field of the single  $\text{Fe}_3\text{O}_4$  layer. In addition, the in-plane magnetic easy directions are rotated by  $45^\circ$  from  $\langle 110 \rangle$  to  $\langle 100 \rangle$ .

As stated above, the azimuthal angle  $\alpha$  of the samples has been varied with respect to the external magnetic field to obtain more insight into the crystalline magnetic anisotropy. Fig.8 compares angular-dependent data (polar plots) of the coercive field  $H_c$  for a  $\text{Fe}_3\text{O}_4/\text{MgO}(001)$  sample and a  $\text{Fe}_3\text{O}_4/\text{NiO}/\text{MgO}(001)$  structure with identical thickness of the  $\text{Fe}_3\text{O}_4$  film. The coercive field changes with the azimuthal angle for both samples showing maxima and minima for distinct directions. For all azimuthal directions, the coercive field is larger for  $\text{Fe}_3\text{O}_4/\text{NiO}$  bilayer than for the corresponding  $\text{Fe}_3\text{O}_4$  single layer.

Maximum coercive fields  $H_c^{\text{max}}$  and minimum coercive fields  $H_c^{\text{min}}$  correspond to magnetic easy and hard in-plane directions. Therefore, Fig.8 shows that magnetic easy directions are in-plane  $\langle 110 \rangle$  directions for  $\text{Fe}_3\text{O}_4/\text{MgO}(001)$  while they are rotated by  $45^\circ$  for  $\text{Fe}_3\text{O}_4/\text{NiO}/\text{MgO}(001)$  pointing into  $\langle 100 \rangle$  directions. On an atomic level, these directions are caused by the magnetic interaction in the single crystalline films. Since the intermediate NiO film is the main difference between both samples, it seems that the different magnetic interaction at the interface  $\text{Fe}_3\text{O}_4/\text{MgO}(001)$  and  $\text{Fe}_3\text{O}_4/\text{NiO}(001)$  causes this modification. Compared to other systems, e.g., based on  $\text{SrTiO}_3$  substrates,<sup>27</sup> we believe that strain effects are less important here since the vertical distortion of both films  $\text{Fe}_3\text{O}_4$  and  $\text{NiO}$  is less than 1% (cf. Fig.6).

An overview over the azimuthal dependence of the coercive field for different single layers and bilayers is presented in Fig.9 varying the thickness of the oxide films. On one hand, one can again easily distinguish between single  $\text{Fe}_3\text{O}_4$  layers with low coercive fields and  $\text{Fe}_3\text{O}_4/\text{NiO}$  bilayers with increased coercive fields. On the other hand, the coercive fields of some samples depend on the azimuthal angle (anisotropic in-plane behavior) while they do not for others (isotropic in-plane behavior). It is reasonable that this effect may be related to the thickness of the  $\text{Fe}_3\text{O}_4$  film.

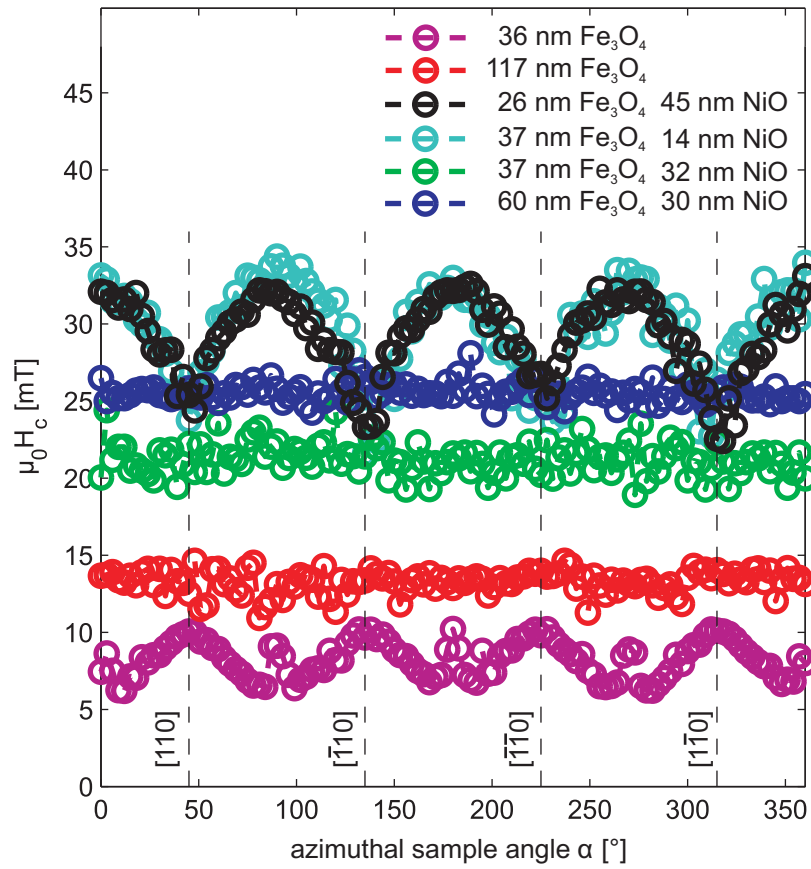


Figure 9. Comparison of the azimuthal dependence of the coercive field of various samples (structure presented in Tab.1). Single Fe<sub>3</sub>O<sub>4</sub> layers have a smaller coercive field than Fe<sub>3</sub>O<sub>4</sub>/NiO bilayers. Both kind of structures show samples with isotropic (constant coercive field) and with anisotropic behaviour (periodically varying coercive field).

For the single Fe<sub>3</sub>O<sub>4</sub> film, we obtain an anisotropic behavior for the 36nm film thickness while the coercive field is isotropic for the thicker 117nm film. We observed a gradual disappearance of the anisotropy with increasing film thickness also for other samples (not shown here). This effect may be attributed to the fact that the in-plane pinning of the magnetization due to the shape anisotropy decreases with increasing film thickness.

For the Fe<sub>3</sub>O<sub>4</sub>/NiO(001) bilayers, however, the situation is much more complicated. On the one hand, we observe anisotropic behavior for sample C (26nm Fe<sub>3</sub>O<sub>4</sub>, 45nm NiO) as well as sample D (37nm Fe<sub>3</sub>O<sub>4</sub>, 14nm NiO). On the other hand, the other bilayer samples E (37nm Fe<sub>3</sub>O<sub>4</sub>, 32nm NiO) and F (60nm Fe<sub>3</sub>O<sub>4</sub>, 30nm NiO) show isotropic behavior. Considering sample F with 60nm Fe<sub>3</sub>O<sub>4</sub> film thickness, it seems that the disappeared anisotropy can also be attributed to the increased Fe<sub>3</sub>O<sub>4</sub> film thickness. Comparing sample D and E, however, we also observe the loss of anisotropy for an increased NiO film thickness. Contrary to this, sample C shows anisotropic behavior for a thick NiO film (film thickness 45nm) while the Fe<sub>3</sub>O<sub>4</sub> film thickness (26nm) is only slightly reduced. Thus, the magnetic anisotropy or isotropy of the Fe<sub>3</sub>O<sub>4</sub> films does not depend only on the thickness of these films or of the NiO buffer films but additional effects seem to play an important role.

Therefore, further investigations are necessary to shed more light on the influence of the crystalline structure of bilayers on the magnetic behavior of Fe<sub>3</sub>O<sub>4</sub> films. In particular, experiments with Ferro Magnetic Resonance (FMR) are planned to determine anisotropic crystal fields in detail.

## 4. CONCLUSION

Here, we demonstrated that  $\text{Fe}_3\text{O}_4/\text{NiO}$  bilayers can be formed by RMBE if adequate deposition conditions (deposition temperature, oxygen pressure, growth rate) are used. The surface near region of the single oxide films were examined *in-situ*. They showed the aimed stoichiometry and well ordered surface structures. Complete structure were studied *ex-situ* by means of synchrotron radiation. On one hand, the thinnest  $\text{Fe}_3\text{O}_4$  films showed tensile strain which gradually relaxed with increasing film thickness. On the other hand, the NiO films showed always tensile strain and did not relax. Furthermore, the different interfaces were very smooth as necessary for spintronic applications. The magnetic behavior of the bilayers was very complex showing partly in-plane crystalline magnetic anisotropy partly not. The in-plane pinning of the magnetization decreases with increasing film thickness. In summary, we demonstrated that appropriate  $\text{Fe}_3\text{O}_4/\text{NiO}$  bilayers can be formed on  $\text{MgO}(001)$ . Since it is well-known that single  $\text{Fe}_3\text{O}_4$  films have also excellent properties if grown on  $\text{MgO}(001)$ , combining both result, it seems accessible that complete  $\text{Fe}_3\text{O}_4/\text{MgO}/\text{Fe}_3\text{O}_4/\text{NiO}/\text{MgO}(001)$  TMJs can be built in the near future.

## ACKNOWLEDGMENTS

Parts of this research were carried out at the light source PETRA III at DESY, a member of the Helmholtz Association (HGF). We would like to thank O. H. Seeck for assistance using beamline P08. Financial support by the DFG (KU2321/2) is gratefully acknowledged.

## REFERENCES

- [1] Marhoun, F. and Kanji, Y., "High quality  $\text{Fe}_{3\delta}\text{O}_4/\text{InAs}$  hybrid structure for electrical spin injection," *Appl. Phys. Lett.* **90**, 112501 (2007).
- [2] Bibes, M., Villegas, J. E., and Barthelémy, A., "Ultrathin oxide films and interfaces for electronics and spintronics," *Adv. Phys.* **60**, 5 (2011).
- [3] Julliere, M., "Tunneling between ferromagnetic films," *Phys. Lett.* **A54**, 225 (1975).
- [4] Moodera, S., Kinder, L. R., Wong, T. M., and Meservey, R., "Large magnetoresistance at room-temperature in ferromagnetic thin-film tunnel-junctions," *Phys. Rev. Lett.* **74**, 3273 (1995).
- [5] Miyazaki, T. and Tezuka, N., "Giant magnetic tunneling effect in  $\text{Fe}/\text{Al}_2\text{O}_3/\text{Fe}$  junction," *J. Magn. Magn. Mater.* **139**, L231 (1995).
- [6] Moodera, S. and Kinder, L. R., "Ferromagnetic-insulator-ferromagnetic tunneling: Spin-dependent tunneling and large magnetoresistance in trilayer junctions," *J. Appl. Phys.* **79**, 4724 (1996).
- [7] Marnitz, L., Rott, K., Niehörster, S., Klewe, C., Meier, D., Fabretti, S., Witzki, M., Krampf, A., Kuschel, O., Schemme, T., Kuepper, K., Wollschläger, J., Thomas, A., Reiss, G., and Kuschel, T., "Sign change in the tunnel magnetoresistance of  $\text{Fe}_3\text{O}_4/\text{MgO}/\text{Co-Fe-B}$  magnetic tunnel junctions depending on the annealing temperature and the interface treatment," *AIP Advances* **5**, 047103 (2015).
- [8] Gatel, C., Snoeck, E., Serin, V., and Fert, A. R., "Epitaxial growth and magnetic exchange anisotropy in  $\text{Fe}_3\text{O}_4/\text{NiO}$  bilayers grown on  $\text{MgO}(001)$  and  $\text{Al}_2\text{O}_3(0001)$ ," *Eur. Phys. J.* **B45**, 157 (2005).
- [9] Schemme, T., Kuschel, O., Kuepper, F. B. K., and Wollschläger, J., "Structure and morphology of epitaxially grown  $\text{Fe}_3\text{O}_4/\text{NiO}$  bilayers on  $\text{MgO}(001)$ ," *Thin Solid Films* **589**, 526 (2015).
- [10] Bertram, F., Deiter, C., Hoefert, O., Schemme, T., Timmer, F., Suendorf, M., Zimmermann, B., and Wollschläger, J., "X-ray diffraction study on size effects in epitaxial magnetite thin films on  $\text{MgO}(001)$ ," *J. Phys. D: Appl. Phys.* **45**, 395302 (2012).
- [11] Bertram, F., Deiter, C., Schemme, T., Jentsch, S., and Wollschläger, J., "Reordering between tetrahedral and octahedral sites in ultrathin magnetite films grown on  $\text{MgO}(001)$ ," *J. Appl. Phys.* **113**, 184103 (2013).
- [12] Seeck, O. H., Deiter, C., Pflaum, K., Bertram, F., Beerlink, A., Franz, H., Horbach, J., Schulte-Schrepping, H., Murphy, B. M., Greve, M., and Magnussen, O., "The high-resolution diffraction beamline P08 at PETRA III," *J. Synchrotron Rad.* **19**, 130 (2012).
- [13] Schmitt, B., Brönnimann, C., Eikenberry, E., Gozzo, F., Hörmann, C., Horisberger, R., and Patterson, B., "Mythen detector system," *Nucl. Instrum. Methods Phys. Res.* **A501**, 267 (2003).

- [14] Kuschel, T., Bardenhagen, H., Wilkens, H., Schubert, R., Hamrle, J., Pištora, J., and Wollschläger, J., "Vectorial magnetometry using magnetooptic Kerr effect including first- and second-order contributions for thin ferromagnetic films," *J. Phys. D: Appl. Phys.* **44**, 265003 (2011).
- [15] Yamashita, T. and Hayes, P., "Analysis of XPS spectra of  $\text{Fe}^{2+}$  and  $\text{Fe}^{3+}$  ions in oxide materials," *Appl. Surf. Sci.* **254**, 2441 (2008).
- [16] Mansour, A. N., "Characterization of NiO by XPS," *Surf. Sci. Spectra* **3**, 231 (1994).
- [17] Nesbitt, H. W., Legrand, D., and Bancroft, G. M., "Interpretation of Ni2p XPS spectra of Ni conductors and Ni insulators," *Phys. Chem. Minerals* **27**, 357 (2000).
- [18] Klewe, C., Meinert, M., Boehnke, A., Kuepper, K., Arenholz, E., Gupta, A., Schmalhorst, J.-M., Kuschel, T., and Reiss, G., "Physical characteristics and cation distribution of  $\text{NiFe}_2\text{O}_4$  thin films with high resistivity prepared by reactive co-sputtering," *J. Appl. Phys.* **115**, 123903 (2014).
- [19] Fujii, T., de Groot, F. M. F., Sawatzky, G. A., Voogt, F. C., Hibma, T., and Okada, K., "In situ XPS analysis of various iron oxide films grown by  $\text{NO}_2$ -assisted molecular-beam epitaxy," *Phys. Rev.* **B59**, 3195 (1999).
- [20] Chambers, S. A., "Analysis of XPS spectra of  $\text{Fe}^{2+}$  and  $\text{Fe}^{3+}$  ions in oxide materials," *Surf. Sci. Rep.* **39**, 105 (2000).
- [21] Parratt, L. G., "Surface studies of solids by total reflection of x-rays," *Phys. Rev.* **95**, 359 (1954).
- [22] Croce, P. and Neovt, L., "Influence of rough interfaces on specular reflection of x-rays," *J. Appl. Crystallography* **7**, 125 (1974).
- [23] Als-Nielsen, J. and Morrow, D., [*Elements of Modern X-Ray Physics*], Wiley, New York (2001).
- [24] Hashimoto, S., Peng, J.-L., Gibson, W. M., Schowalter, L. J., and Fathauer, R. W., "Strain measurement of epitaxial  $\text{CaF}_2$  on Si(111) by MeV ion channeling," *Appl. Phys. Lett.* **47**, 1071 (1985).
- [25] James, M. A. and Hibma, T., "Thickness-dependent relaxation of  $\text{NiO}(001)$  overlayers on  $\text{MgO}(001)$  studied by x-ray diffraction," *Surf. Sci.* **433-435**, 718 (1999).
- [26] Every, A. G. and McCurdy, A. K., "Table 7. cubic system. binary compounds.," in [*Springer Materials - The Landolt-Börnstein Database*], Nelson, D. F., ed., Springer, Berlin (1992).
- [27] Chen, Y. Z., Sun, J. R., Han, Y. N., Xie, X. Y., Shen, J., Rong, C. B., He, S. L., and Shen, B. G., "Microstructure and magnetic properties of strained  $\text{Fe}_3\text{O}_4$  films," *J. Appl. Phys.* **103**, 07D703 (2008).